PHYSICAL REVIEW FLUIDS **1**, 083201 (2016)

Hemodynamic forces in a model left ventricle

Federico Domenichini*
Department of Civil and Environmental Engineering, University of Firenze, Via S. Marta 3, 50139 Firenze, Italy

Gianni Pedrizzetti†
Department of Engineering and Architecture, University of Trieste, Piazzale Europa 1, 34127 Trieste, Italy
(Received 13 June 2016; published 23 December 2016)

Intraventricular pressure gradients were clinically demonstrated to represent one useful indicator of the left ventricle (LV) function during the development of heart failure. We analyze the fluid dynamics inside a model LV to improve the understanding of the development of hemodynamic forces (i.e., mean pressure gradient) in normal conditions and their modification in the presence of alterations of LV tissue motion. To this aim, the problem is solved numerically and the global force exchanged between blood flow and LV boundaries is computed by volume integration. We also introduce a simplified analytical model, based on global conservation laws, to estimate hemodynamic forces from the knowledge of LV tissue information commonly available in cardiac imaging. Numerical results show that the normal intraventricular gradients feature a deep brief suction at early diastolic filling and a persistent thrust during systolic ejection. In presence of abnormalities of the wall motion, the loss of time synchrony is more relevant than the loss of spatial uniformity in modifying the normal pressure gradient spatiotemporal pattern. The main findings are reproduced in the integral model, which represents a possible easy approach for integrating fluid dynamics evaluations in the clinical examination.

DOI: 10.1103/PhysRevFluids.1.083201

I. INTRODUCTION

Heart failure is the principal social threatening cardiac progressive dysfunction. It presents either as a primary pathology or as a consequence of almost any other primary disease. The clinical syndrome of heart failure is associated with the development of left ventricle (LV) "remodeling," a modification of the ventricular geometry that progressively alters its functional parameters. Despite modern treatments, hospitalization and death rate remain high, with nearly 50% of people diagnosed with heart failure dying within 5 years [1]. Several factors, from genetic to environmental, are involved in the initiation and progression of LV remodeling. Among those, the alteration of cardiac mechanics accompanies the pathologic development, although it cannot be said whether as a participating cause or as a consequence. The biomechanical effects that could lead to LV remodeling are mainly ascribed to the alteration of stresses on the myocardial fibers, which stimulates the growth and multiplication of cells, giving rise to an increase of muscular thickness (LV hypertrophy) or extension (LV dilatation) [2,3]. However, this picture is not consistently predictive of the future risk of cardiac remodeling. For example, it does not explain how small changes occurring at early stages of a disease, whose associated stresses are well within the physiological range, may provoke large progressive modifications nor does it clarify how a regional disease rapidly remodels the entire ventricular chamber [4,5].

There is growing evidence that changes of the intraventricular fluid dynamics are observable during the process of cardiac remodeling and that these may even influence its progression [6,7]. Indeed, blood flow inside the LV is an intense phenomenon characterized by velocities above 1 m/s, in a cavity of a few centimeters, subjected to accelerations and/or decelerations lasting a

*federico.domenichini@unifi.it
†giannip@dia.units.it

fraction of a second. Several studies provided evidence that flow in the LV is characterized by the formation of vortices, which smoothly accompany the unsteady blood motion from the mitral entrance to the backward-facing outflow tract and can be altered in the presence of pathologies [8,9]. In parallel, clinical studies demonstrated the existence of a relationship between flow and cardiac function [10–13]. Following these and numerous other works, some preliminary results revealed the potential significance of blood motion to the modulation of adverse clinical outcome in heart failure patients [14]. However, despite this progress, understanding the possible relationship between cardiac flow and progressive remodeling is still largely incomplete.

From a biomechanical perspective, a progressive cardiac pathology typically starts with minor alterations in the contraction-expansion cycle of the LV walls that may then lead to global dysfunctions. Such initial changes are local and short lasting. However, they affect the entire LV through blood: an incompressible medium that fills the chamber and keeps the various tissue regions in direct contact, allowing exchange of momentum between them. Flow-mediated forces are sensed, in terms of the shear pressure difference, at the cellular level on the endocardial boundary. Although the causal chain of events remains elusive, combined observations at different scales suggest that flow-induced stresses, at untimed instants and on improper regions, induce a physiological feedback, which stimulates the cardiac adaptation [15,16]. This feedback is always active to comply with normal functional changes such as during exercise or a disease. Under some circumstances, however, adaptation may not settle into a physiologically stable state and slowly progresses toward large-scale remodeling and eventually heart failure [6,7].

In any case, blood flow can interact with tissue solely through the spatial distribution of wall stresses or, in integral terms, through hemodynamic forces. In healthy LVs the intraventricular pressure gradients, which contribute to most of such forces, are aligned along the base-apex direction to reflect the natural emptying-filling dynamics. This was confirmed *in vivo* by mean of echocardiography [17] and by magnetic resonance imaging [18]. The same magnetic resonance study also showed that in remodeled dilated hearts, the average hemodynamic forces lose their longitudinal orientation and develop transversal components of comparable amplitude. A recent echocardiographic study [19] demonstrated that patients expected to develop cardiac remodeling exhibit growth of the transversal component of hemodynamic forces well before remodeling has started.

In summary, LV blood dynamics is characterized by a nonsymmetric flow, with formation of vortices that interacts with the moving walls. Under normal conditions, such flow is associated with approximately longitudinal intraventricular forces, while nonphysiological asymmetric transversal components develop in dysfunctional hearts only. The deviation of hemodynamic forces represents a large-scale, clinically measurable mechanical outcome associated with an abnormal biomechanical blood-tissue interaction.

This study explores the relationship between LV tissue motion and fluid dynamics, verifying how changes in the former are reflected in terms of hemodynamic forces. This study does not investigate how LV remodeling modifies flow forces. It explores how small differences in LV tissue dynamics, which may or may not evolve toward heart failure, are reflected in terms of flow forces. It aims to start providing a physics-grounded reference for future clinical studies looking for associations between cardiac hemodynamic and potential early indicators of heart failure in different pathologies. To this purpose, we introduce a model of LV geometry that is simple enough yet realistic for drawing average results that can be valid beyond subject-specific individualities. Controlled changes in LV tissue dynamics are imposed and the fluid dynamics therein is reproduced by direct numerical simulations of the Navier-Stokes equations. Results show that the lack of synchrony of the wall motion alters the orientation of intraventricular forces more than the reduction of its amplitude.

This study also introduces an approximate integral model for estimating the intraventricular hemodynamic forces, aimed to reproduce the principal modification of the dynamical coupling between blood and tissue associated with changes in wall motion. The model has several limitations: It cannot reproduce higher-frequency sharp phenomena that are associated with the details of intraventricular vortex dynamics; it also uses some assumptions of geometrical symmetry that apply in the present numerical study and have to be removed before moving to clinical applications. However,

developments based on such an approximate model could permit preliminary evaluations of LV fluid dynamics, in global terms, through the information normally recorded in cardiac imaging before the need of introducing complex diagnostic techniques for recording three-dimensional (3D) flow fields.

II. MATHEMATICAL DEFINITIONS: THE LV MODEL

A. The LV geometry

Let us preliminarily consider a generalized ellipsoidal surface described in Cartesian coordinates as

$$x_e(\varphi,\theta,t) = R_e(\theta,t)\sin\varphi\cos\theta, \quad y_e(\varphi,\theta,t) = R_e(\theta,t)\sin\varphi\sin\theta, \quad z_e(\varphi,\theta,t) = \tfrac{2}{3}H(t)(1-\cos\varphi), \tag{1}$$

where θ and φ are the parametric circumferential and longitudinal coordinates on the surface, respectively, $0 \leqslant \theta \leqslant 2\pi$ and $0 \leqslant \varphi \leqslant 2\pi/3$. The function $H(t)$ represents the ellipsoid height from the apex $z(0,\theta,t) = 0$ to the valvular plane at $z_v\,(\frac{2\pi}{3},\theta,t) = H(t)$; t is the time. The radius $R_e(\theta,t)$ at the equatorial plane $\varphi = \pi/2$ is modulated along θ with a simple sinusoidal shape that breaks the symmetry with respect to the plane $x = 0$ and still remains symmetric with respect to the plane $y = 0$ containing the centers of the mitral and aortic orifices

$$R_e(\theta,t) = \left[\frac{R_0}{2} + \frac{R_1+R_2}{4} + \frac{R_1-R_2}{2}\cos\theta + \left(\frac{R_1+R_2}{4} - \frac{R_0}{2}\right)\cos 2\theta\right] \tag{2}$$

where $R_0(t), R_1(t)$, and $R_2(t)$ are functions of time only. Notice that when R_e is allowed to vary with θ, the system of coordinates $[\theta,\varphi]$ is not orthogonal on the surface.

The surface (1) is a good representation of an average regular LV geometry during the entire heartbeat in most of the ventricle. However, approaching the mitral region, which is located just above $\varphi = 2\pi/3$, the surface has to match the approximately circular shape of the valvular plane, which is surrounded by a fibrous annulus and does not changes appreciably over time. Calling R_v the radius of the valve-containing annulus, considered flat for simplicity, its coordinates are

$$x_v = R_v\cos\theta, \quad y_v = R_v\sin\theta, \quad z_v = H(t). \tag{3}$$

We thus consider a more realistic LV endocardial surface x_w given by the ellipsoidal surface (1) up to the equator level $\varphi = \pi/2$ and then progressively modulated to eventually match the valvular contour (3) at $\varphi = 2\pi/3$. This is obtained by an expression formally similar to (1),

$$\begin{aligned} x_w(\varphi,\theta,t) &= R(\theta,\varphi,\,t)\sin\varphi\cos\theta, \\ y_w(\varphi,\theta,t) &= R(\theta,\varphi,\,t)\sin\varphi\sin\theta, \\ z_w(\varphi,\theta,t) &= \tfrac{2}{3}H(t)(1-\cos\varphi), \end{aligned} \tag{4}$$

where the radial function $R(\theta,\varphi,\,t)$ is equal to the expression (2) below the equator and smoothly connects to the valvular plane constant value R_v above it:

$$R(\theta,\varphi,t) = \begin{cases} R_e(\theta,t), & 0 \leqslant \varphi \leqslant \frac{\pi}{2} \\ R_e(\theta,t)[1-w(\varphi)] + \frac{2}{\sqrt{3}}R_v w(\varphi), & \frac{\pi}{2} \leqslant \varphi \leqslant \frac{3}{2}\pi. \end{cases} \tag{5}$$

The modulation is achieved by the arbitrary weighting function

$$w(\varphi) = \left(\frac{6\varphi}{\pi} - 3\right)^2,$$

which ranges from zero to unity when φ ranges from $\pi/2$ to $2\pi/3$ and has zero derivative at $\varphi = \pi/2$, ensuring a smooth continuation from the ellipsoidal surface (1). Figure 1 shows the resulting geometry for an exemplary case.

The LV geometry is thus defined by the longitudinal function $H(t)$ describing its height, the fixed value R_v of the valvular annulus, and the radial functions $R_0(t), R_1(t)$, and $R_2(t)$ in Eq. (2). Here $R_1(t)$ and $R_2(t)$ are the radial distances at the equator below the mitral and aortic orifices,

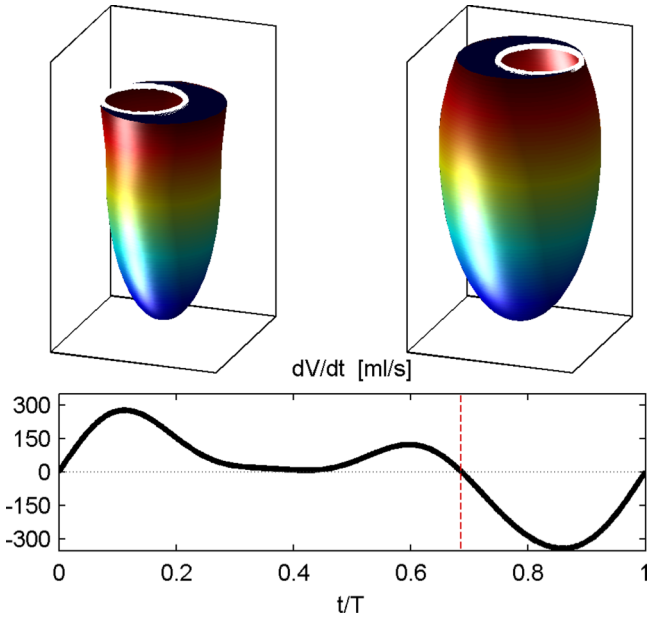

FIG. 1. Exemplary view of the LV surface at the end of the systolic (top left) and diastolic (top right) phases. Shown on the bottom is the ventricular flow rate, healthy reference case (No. 0 in Table I). Positive and negative values correspond to diastole and systole, respectively.

respectively, and $R_0(t)$ is the distance in the opposite transversal plane $x = 0$. All the functions are periodic with the heartbeat period T. The volume of the LV can be computed from (4) as

$$V(t) = H\left[a_1 \frac{\left(12R_0^2 + 7R_1^2 + 7R_2^2 + 4R_0R_1 + 4R_0R_2 - 2R_1R_2\right)}{32} + a_2 \frac{R_v(2R_0 + R_1 + R_2)}{4} + a_3 R_v^2\right], \tag{6}$$

where the three coefficients a_1,a_2, and a_3 can be easily estimated via analytical integration of the expressions above (to eventually give $a_1 \approx 1.9485$, $a_2 \approx 0.2832$, and $a_3 \approx 0.2165$). In Eq. (6) and hereinafter the time dependence is omitted for brevity, except when it is useful for clarity.

B. Model parameters in a normal reference case

Under normal conditions, horizontal LV sections are approximately circular and the LV geometry is axially symmetric: $R_0 = R_1 = R_2$. A normal LV has a shape at end-systole (assumed here as $t = 0$) that is nearly cylindrical, or slightly tapered, on its upper portion. This gives a radius at the base R_v that is close to the value of the mean equatorial radius $R_0(0)$. At the same instant, the LV height is approximately twice the LV width, a ratio that decreases during diastole when the LV chamber becomes wider. In the present case, we thus assume the ratio $R_v/R_0(0) = 1.1$ to mimic the slightly wider valvular plane found at end-systole and the ratio $H(0)/R_0(0) = 4$; these parameters are those used for Fig. 1.

A large variety of choices remains to specify the time profiles of $H(t)$ and $R_0(t)$. The temporal variation of these two functions is relatively similar, but not self-similar, and their ratio is not constant. A simple argument based on the hypothesis of linear elastic membrane deformation at the equatorial plane [20] suggested the relationship

$$\frac{dR_0}{R_0} = \frac{dH}{H}\left(2 - \frac{9}{4}\frac{R_0^2}{H^2}\right). \tag{7}$$

The relation (7) is consistent, on average, with measurements from imaging and presents the correct behavior of decreasing the ratio H/R_0 from systole to diastole. Combination of (6) and (7) gives

$$\frac{dV}{dt} = R_0^2\left[a_1 + a_2\frac{R_v}{R_0} + a_3\left(\frac{R_v^2}{R_0^2}\right) + \left(2 - \frac{9}{4}\frac{R_0^2}{H^2}\right)\left(2a_1 + a_2\frac{R_v}{R_0}\right)\right]\frac{dH}{dt}. \tag{8}$$

The volume curve $V(t)$ is the quantity that is commonly measured in most echocardiographic examinations. Once this curve is specified, it is thus possible to integrate (8) and (7) and estimate the time variation of the LV length H and width R_0 if they are known at the initial instant (end-systole). In practice, the knowledge of the end-systolic volume $V(0)$, in combination with the ratios $H(0)/R_0(0)$ and $R_v/R_0(0)$, gives the end-systolic values of $H(0)$ and $R_0(0)$ from (6). These values are taken as initial conditions and integrated in time to obtain the functions $H(t)$ and $R_0(t)$ using (7) and (8).

We measured the volume curves from a series of normal subjects (from triplane and 3D echocardiography) and built an approximate normal profile in a time Fourier series

$$V(t) = V_0 + \sum_{k=1}^{4} V_k e^{ik2\pi(t/T)} + \text{c.c.},$$

with coefficients $V_k = [96, -12 + 3.5i, -7\text{–}1.5i, -0.8\text{–}0.6i, -0.2 + 0.3i]$ for $k = 0$–4, where the notation c.c. stands for complex conjugate and the dimension of the numeric values is in cm^3. This volume curve corresponds to an average normal profile with end-systolic and end-diastolic volumes equal to 56 and 123 cm^3, respectively, and the ejection fraction (EF), the difference between these two volumes relative to the maximum value, is equal to 55%. This volume profile also ensures normal values for other clinical parameters such as the ratio E/A between the peak velocities during the two diastolic filling waves (early filling and atrial contraction) of about 2.3 and a value of the global longitudinal strain of about -20%.

The geometric definition of the problem is completed by that of the mitral and aortic orifices. The dynamics of mitral leaflets has a direct influence on the intraventricular flow pattern and therefore on the associated forces. Recent literature introduced numerical techniques for uncoupled or weakly coupled models of mitral leaflets [21,22]. However, the present study seeks the relationship between forces and LV wall motion, and results in the presence of a mitral model may be influenced by its details and parameters. In order to limit the number of degrees of freedom, we avoid modeling the valvular leaflets whose influence is beyond the scope of the present study. We thus consider a simple opening and closing behavior of the orifices having fixed circular shapes defined by their radii R_{mv} and R_{ao} and by the x positions of their centers in the plane $y = 0$,d_{mv} and d_{ao}. In what follows, we assume $R_{mv} = R_{ao} = 2R_v/3$ and $d_{mv} = -d_{ao} = R_v/3$. In fluid dynamics terms, these properties correspond to a diastolic Reynolds number $\mathrm{Re} = UD/\nu \cong 4000$, where U is the peak mean velocity across the mitral orifice of diameter $D = 2R_{mv}$ and ν is the kinematic viscosity, to a Strouhal number $\mathrm{St} = D/UT \cong 5 \times 10^{-2}$, and a vortex formation time equal to $\frac{1}{D}\int_{Amv} U(t)dt \cong 3.5$, a little below the limit for the optimal value of 4 [11] (see Table I).

III. MATHEMATICAL DEFINITION: FLOW ANALYSIS

A. Numerical solution of the fluid problem

We assume the blood to be a Newtonian fluid, with kinematic viscosity $v = 3.3 \times 10^{-2}$ cm^2/s and density $\rho = 1.05$ g/cm^3. The Navier-Stokes and continuity equations in dimensional form

$$\frac{\partial \boldsymbol{v}}{\partial t} + \boldsymbol{v}\cdot\nabla\boldsymbol{v} = -\frac{1}{\rho}\nabla p + \nu\nabla^2\boldsymbol{v}\,, \tag{9}$$

$$\nabla\cdot\boldsymbol{v} = 0 \tag{10}$$

are solved numerically, where $\boldsymbol{v}$ is the velocity vector field and p is the pressure including gravity.

The moving LV boundary defined above is placed inside a computational box, which is periodic along the x and y directions, and the imposed endocardial motion (4) drives the flow solution.

TABLE I. List of simulations and associated dimensionless parameters: Re, Reynolds number; St, Strouhal number; VFT, vortex formation time; and EF, ejection fraction. Refer to the text for a complete description of the parameters used in the different cases.

No.	Short description	Re	St	VFT	EF
0	reference case	4.1×10^3	5.1×10^{-2}	3.47	55%
1	reduced motion: R_1 halved	3.7×10^3	5.5×10^{-2}	3.17	51%
2	reduced motion: R_2 halved	3.7×10^3	5.5×10^{-2}	3.17	51%
3	reduced motion: $R_1 = 0$	3.4×10^3	6.1×10^{-2}	2.85	47%
4	reduced motion: $R_2 = 0$	3.4×10^3	6.1×10^{-2}	2.85	47%
5	reduced motion: H, R_0, R_2 halved, $R_1 = 0$	1.9×10^3	10.4×10^{-2}	1.66	26%
6	asynchrony: R_1 delayed $T/8$	3.6×10^3	5.7×10^{-2}	3.20	50%
7	asynchrony: R_1 anticipated $T/8$	3.2×10^3	6.4×10^{-2}	3.02	50%
8	asynchrony: septal flash	4.1×10^3	5.1×10^{-2}	3.47	55%

The numerical method is that reported and employed in previous works [12,21,23,24]. Briefly, the Navier-Stokes equation is advanced in time using an explicit third-order Runge-Kutta scheme and second-order finite differences for the spatial discretization. Mass conservation is then enforced by solving the Poisson-type problem for the irrotational correction to the velocity. This second step is performed in the Fourier space, given the biperiodicity of the computational box, which ensures a high computational efficiency. The presence of the forcing motion of the LV surface is accounted for through an immersed boundary element method [25].

The results reported here have been obtained using a dimensional domain $L_x = L_y = 8$ and $L_z = 12$, with the dimensions in centimeters. Following the above-reported considerations about the LV geometry, the R_v length scale is approximately 1.95 cm. A typical grid size is $N_x \times N_y \times N_z = 128^2 \times 192$. The time step is set to $\Delta t = T/2048$. The LV surface is defined by $N_\theta \times N_\varphi$ Lagrangian points ensuring a spatial description finer than the Cartesian grid resolution. The same number of points is used to describe the closed part of the valvular plane. Flow starts from at rest $t = 0$; results are reported for the third heartbeat, which was verified to be periodic and independent of the initial condition.

B. Computation of hemodynamic forces

The total hemodynamic force vector exchanged between the blood and the LV boundary can be obtained through (9) by the integral

$$\boldsymbol{F}(t) = \int_{V(t)} \left(\frac{\partial \boldsymbol{v}}{\partial t} + \boldsymbol{v} \cdot \boldsymbol{\nabla} \boldsymbol{v} \right) \rho \, dV, \tag{11}$$

which can be evaluated from the numerical solutions of the velocity field. The expression (11) allows us to estimate the integral forces, avoiding the numerical difficulty arising in the evaluation of the instantaneous pressure field close to the LV wall [17,19,26].

IV. INTEGRAL MODEL FOR ESTIMATING HEMODYNAMIC FORCES

The hemodynamic forces can also be evaluated from the integral balance of momentum

$$\boldsymbol{F}(t) = \int_{V(t)} \rho \frac{\partial \boldsymbol{v}}{\partial t} dV + \int_{S(t)} \rho \boldsymbol{v} (\boldsymbol{v} \cdot \boldsymbol{n}) dS, \tag{12}$$

where $V(t)$ and $S(t)$ are the instantaneous volume and boundary surface of the LV flow domain, respectively, and $\boldsymbol{n}$ is the outward unit normal vector. The two integrals on the right-hand side of (12) are the inertial and convective terms, respectively, that correspond to the same terms in Eq. (11).

Hemodynamic forces depend on the details of the intraventricular flow (11), which is characterized by the presence of vorticity [27,28]; however, a large part of the global dynamics can be presumably imputable to the bulk flow. We introduce here a model to estimate the integrals in Eq. (12) from global properties without using the solution of the velocity field inside the LV. The objective is to provide an approximate evaluation of the forces, on the basis of physical principles, in the absence of the knowledge of the intracavity blood motion and using low-dimensional data that can be normally measured in clinical practice.

A. Inertial term

Calculation of the inertial term, the first term on the right-hand side of (12), requires a mean to estimate the spatial average velocity $\boldsymbol{U}(t)$ in the LV cavity. In cylindrical coordinates, the velocity components can be expresses in a Fourier series as (keeping the leading terms only and omitting the dependence on the time t)

$$v_z(z,r,\theta) = v_z^{(0)}(z,r) + v_z^{(1)}(z,r)\cos\theta + \cdots, \tag{13a}$$

$$v_r(z,r,\theta) = v_r^{(0)}(z,r) + v_r^{(1)}(z,r)\cos\theta + \cdots, \tag{13b}$$

$$v_\theta(z,r,\theta) = v_\theta^{(1)}(z,r)\sin\theta + \cdots. \tag{13c}$$

The superscripts stand for the harmonics along azimuthal coordinate θ. The above expressions take into account the symmetry of the flow about the y axis. This symmetry is present in the geometric model adopted here; however, such symmetry is lost in real LVs and this simplification should be removed when extending such a model for clinical applications.

It is evident that the z component of the LV-averaged velocity $U_z(t)$ is due to the zeroth harmonic only. For this harmonic, the continuity equation written at any level z, of known area $A(z,t)$,

$$\frac{d}{dz}\left[v_z^{(0)}A(z,t)\right] = -\frac{dA(z,t)}{dt}, \tag{14}$$

allows the evaluation of the average velocity at each level. Then the average velocity of the entire LV can be written as

$$U_z(t) = \frac{1}{V(t)}\int_0^{H(t)}\left\{\int_0^z \frac{dA(s,t)}{dt}ds\right\}dz. \tag{15}$$

It is worth remarking that dimensional arguments suggest expressing (15) as

$$U_z(t) = -\kappa_z(t)\frac{H(t)}{V(t)}\frac{dV(t)}{dt}, \tag{16}$$

where the time-varying positive coefficient κ_z is

$$\kappa_z(t) = \frac{1}{H(t)}\left(\frac{dV(t)}{dt}\right)^{-1}\int_0^{H(t)}\left\{\int_0^z \frac{dA(s,t)}{dt}ds\right\}dz. \tag{17}$$

It is has been found here that this coefficient is approximately constant in time and weakly varying, ranging between 0.33 and 0.36, among all the configurations analyzed. Once the spatially averaged vertical velocity is known by (15), or (16) and (17), the z component of the inertial term can be written as

$$\int_{V(t)}\rho\frac{\partial \boldsymbol{v_z}}{\partial t}dV \cong \rho V(t)\frac{dU_z(t)}{dt}. \tag{18}$$

The estimate of the mean velocity $U_x(t)$ along x requires us to take into account at least the first harmonic in Eq. (13). For this contribute, the continuity equation reads

$$\frac{\partial\left[r v_r^{(1)}(z,r)\right]}{\partial r} + v_\theta^{(1)}(z,r) = -r\frac{dv_z^{(1)}(z)}{dz}. \tag{19}$$

Having in mind that we are looking for average values, we consider in a first approximation the z component of the velocity to be independent of r. This allows writing the simplest nontrivial solution

$$v_r^{(1)} = -c_r r\frac{\partial v_z^{(1)}}{\partial z}, \quad v_\theta^{(1)} = -c_\theta r\frac{\partial v_z^{(1)}}{\partial z}, \tag{20}$$

where c_r and c_θ are order 1 coefficients, such that $2c_r + c_\theta = 1$ to satisfy mass conservation. Moreover, this flow field is driven by the mass balance argument and should have an irrotational nature; the condition of a zero value of the z component of the vorticity field provides the values for the coefficients $c_r = \frac{2}{3}$ and $c_\theta = -\frac{1}{3}$.

Inserting the expressions (20) into (13), with the same approximation, the x component of the velocity field can be written as

$$v_x(r,\theta,z,t) = v_r^{(0)}\cos\theta - r(c_r\cos^2\theta - c_\theta\sin^2\theta)\frac{\partial v_z^{(1)}}{\partial z} + V_{xw}(z,t), \tag{21}$$

which has a nonzero value once integrated over an area at constant z (or φ). The last term in Eq. (21) is added to include the translational motion due to the mean x velocity of the walls at the level z. Inspecting (21), we can write the term $c_r\cos^2\theta - c_\theta\sin^2\theta = \frac{c_r - c_\theta}{2} + \frac{c_r + c_\theta}{2}\cos 2\theta$. These two terms correspond to a velocity field having no y component and to a pair of symmetric circulatory cells whose x component is zero for symmetry when integrated over the area. Therefore, only the first term, proportional to $c_r - c_\theta = 1$, contributes to the average x component of the velocity.

Before integrating (21), it is necessary to provide an estimation of the velocity gradient $\frac{\partial v_z^{(1)}}{\partial z}$. Following (14), we assume a linear decrease of the vertical velocity from the profile at the base to the null value at the apex and a constant gradient

$$\frac{d}{dz}\left[v_z^{(1)}A(z,t)\right] = \frac{v_z^{(1)}[H(t)]A(H)}{H(t)} \tag{22}$$

from which

$$\frac{dv_z^{(1)}}{dz}(t) = v_z^{(1)}[H(t)]\frac{A(H)}{H(t)}\frac{d}{dz}\left(\frac{z}{A(z,t)}\right). \tag{23}$$

This equation requires only the knowledge of the first harmonic of the vertical velocity at the valvular level $v_z^{(1)}[H(t),t]$ at every instant. This can be obtained by assuming a constant in or out velocity inside the orifice and computing the average value at each circumferential position from which the first harmonic is extracted. In a simpler approach, not used here and more appropriate when the orifices do not extend beyond the LV axis, the first harmonic can be estimated crudely as

$$v_z^{(1)}[H(t)] \approx \begin{cases} \frac{-1}{2A_{mv}}\frac{dV(t)}{dt}, & \frac{dV(t)}{dt} > 0 \\ \frac{+1}{2A_{ao}}\frac{dV(t)}{dt}, & \frac{dV(t)}{dt} < 0, \end{cases} \tag{24}$$

where A_{mv} and A_{ao} are the area's mitral and aortic orifices, respectively.

Integration of (21) using (23) provides the velocity averaged over the entire LV

$$\begin{aligned} U_x(t) &= \frac{1}{V(t)}\int_0^{H(t)}\int_{A(z,t)} v_x(r,\theta,z,t)dA\,dz \\ &= -\frac{1}{2V(t)}v_z^{(1)}\frac{A(H)}{H(t)}\int_0^{H(t)}\frac{d}{dz}\left(\frac{z}{A(z,t)}\right)\int_A r\,dA\,dz + \frac{1}{V(t)}\int_0^{H(t)} V_{xw}(z,t)A(z,t)dz. \end{aligned} \tag{25}$$

The last term in Eq. (25) is given by the integral of wall velocities and it can be computed analytically (although not in a compact formula) in the present model.

It is useful to remark here too that the formula (25) can be expressed similarly to (16) as

$$U_x(t) = -\kappa_x v_z^{(1)} + \frac{1}{V(t)} \int_0^{H(t)} V_{xw}(z,t) A(z,t) dz, \tag{26}$$

where κ_x is the positive time-varying coefficient

$$\kappa_x = \frac{1}{2} \frac{1}{V(t)} \frac{A(H)}{H(t)} \int_0^{H(t)} \frac{d}{dz}\left(\frac{z}{A}\right) \int_A r \, dA \, dz = \frac{A(H)}{3V(t)H(t)} \int_0^{H(t)} \left(\bar{R}(z)\sin\varphi - 2z \frac{\partial \bar{R}(z)\sin\varphi}{\partial z}\right) dz. \tag{27}$$

The last equality in Eq. (27) is not valid in general and applies to the simple geometry used in this study only; in this case the mean radius $\bar{R}(z)$ is given by (5), replacing R_e with the mean value $\bar{R}_e = \frac{R_0}{2} + \frac{R_1+R_2}{4}$. This coefficient is approximately constant and equal to about 0.075 in all configurations analyzed here. Then the x component of the inertial term is eventually given by

$$\int_{V(t)} \frac{\partial \boldsymbol{v_x}}{\partial t} dV \cong \rho V(t) \frac{dU_x(t)}{dt}, \tag{28}$$

which, together with (18), completes the inertial contribution to hemodynamic forces.

B. Convective term

The convective term [second term on the right-hand side of (12)] can be evaluated from the knowledge of the velocity distribution on the lateral wall surface S_{lat} and on the valvular plane surface S_v of the entire LV boundary $S = S_{\text{lat}} \cup S_v$. The velocity of the lateral walls is usually estimable by cardiac imaging methods. In the present model, it is given by time differentiation of (4):

$$v_{xw} = \frac{\partial R(\theta,\varphi,t)}{\partial t} \sin\varphi\cos\theta, \quad v_{yw} = \frac{\partial R(\theta,\varphi,t)}{\partial t} \sin\varphi\sin\theta, \quad v_{zw} = \frac{2}{3} \frac{dH(t)}{dt}(1-\cos\varphi). \tag{29}$$

The expression of the normal vector $\boldsymbol{n}$ can also be computed from the instantaneous surface geometry (4) to give the flux of momentum on the lateral wall

$$\int_{S_{\text{lat}}} \boldsymbol{v}(\boldsymbol{v}\cdot\boldsymbol{n}) dS = \int_{S_{\text{lat}}} \boldsymbol{v_w}(\boldsymbol{v_w}\cdot\boldsymbol{n}) dS. \tag{30}$$

On the valvular plane, velocities are also often estimable from imaging methods and the convective term defined by an expression like (30) can be integrated on the S_v surface. In the present model, the normal is $n = [0\ 0\ 1]$ and the z component of the velocity can be expressed through (13a) with $v_z^{(0)}[H(t)] = \frac{dH}{dt} - \frac{1}{\pi R_v^2} \frac{dV(t)}{dt}$ and $v_z^{(1)}(H)$ [see Eq. (24)]. Therefore, the convective contribution to the vertical velocity is

$$\int_{S_v} v_z(\boldsymbol{v}\cdot\boldsymbol{n}) dS \cong \left(v_z^{(0)^2} + \frac{1}{2} v_z^{(1)^2}\right) \pi R_v^2, \tag{31}$$

where, in general, πR_v^2 stands for the area of the valvular plane, here assumed as circular. The horizontal contribution comes from the product of the vertical velocity (13a) and the x velocity, which is given in Eq. (21). This can be rewritten, ignoring the terms that give eventually zero when multiplied and integrated, as

$$\begin{aligned} v_x(r,\theta,H) &= -r \left.\frac{\partial v_z^{(0)}}{\partial z}\right|_{z=H} \cos\theta - \frac{r}{2} \left.\frac{\partial v_z^{(1)}}{\partial z}\right|_{z=H} \\ &= r v_z^{(0)}(H) \frac{1}{A(H)} \frac{dA}{dz} \cos\theta + \frac{r}{2} v_z^{(1)}(H) \left(\frac{1}{A(H)} \frac{dA}{dz} - \frac{1}{H}\right). \end{aligned} \tag{32}$$

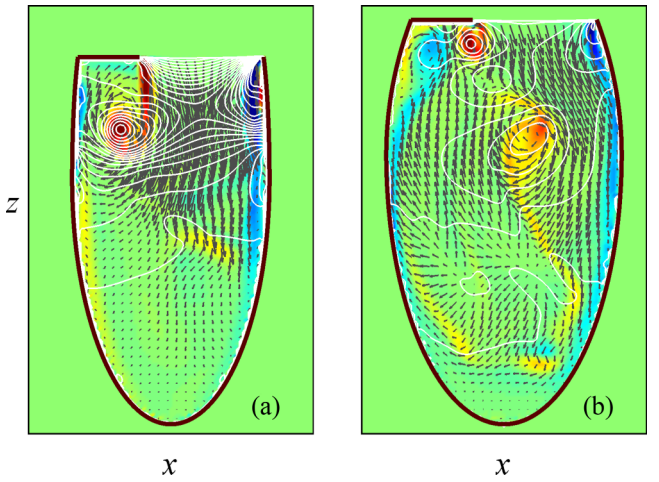

FIG. 2. Flow field in the reference axisymmetric case. Normal vorticity and in-plane velocity fields are shown on the symmetry plane $y = 0$. Snapshots are at (a) diastolic peak ($t = T/8$) and (b) late diastole ($t = 5/8T$). Vorticity is color coded for values in the interval $[-200,200]\mathrm{s}^{-1}$, from blue to red. Velocity vectors are down sampled with respect to the computational grid and scaled, to enhance readability. For the pressure field, white isolines are sampled with a pressure difference equal to 10 Pa.

Multiplication of the z and x components of the velocity and integration on the valvular plane gives

$$\int_{S_v} v_x(\boldsymbol{v}\cdot\boldsymbol{n})ds \cong \frac{1}{3}v_z^{(0)}v_z^1\left(\frac{2R_v}{A}\frac{dA}{dz}-\frac{R_v}{H}\right)\pi R_v^2, \tag{33}$$

where, in the present geometry,

$$\frac{2R_v}{A}\frac{dA}{dz} = 4\frac{d\bar{R}\sin\varphi}{dz} = 4\left[\frac{R_v}{H}\left(\frac{12\sqrt{3}}{\pi}-1\right)-\frac{1}{H}\left(\frac{R_0}{2}+\frac{R_1+R_2}{4}\right)\frac{18}{\pi}\right].$$

It must be remarked that (32) and (33) are based on conservation of mass only and do not take into account the vorticity-driven flow inside the LV. This estimation represents the bulk flow traveling from the inlet to the outlet and it is certainly not accurate during late diastole and early systole, when the horizontal velocity is presumably directed in the opposite direction due to the vortex inside the LV, an effect that cannot be taken into account by global arguments only.

This model does not provide an estimation of the y component of the force that is exactly zero for the assumed symmetry. In addition, it also makes some implicit assumptions on the regularity of the LV geometry; primarily, the valvular plane is assumed to be flat with downward directed inflow and upward directed outflow and the cross section regular enough to allow a single harmonic representation of the flow. These apply to the present study but require revision before applying the model in a more general clinical context.

V. RESULTS

A. Normal reference case

The flow computed in the reference healthy case, No. 0 in Table I, is consistent with the findings about the normal intraventricular flow previously reported in the literature [8,9]. Two instants of the flow evolution are reported in Fig. 2 on the symmetry plane $y = 0$ in terms of orthogonal vorticity, in-plane velocity distributions, and isolines of relative pressure. The diastole is characterized by a steep velocity gradient at the inlet and the formation of a compact vortex ring structure during the early filling phase. On the lateral wall, below the mitral orifice, such a structure interacts with the

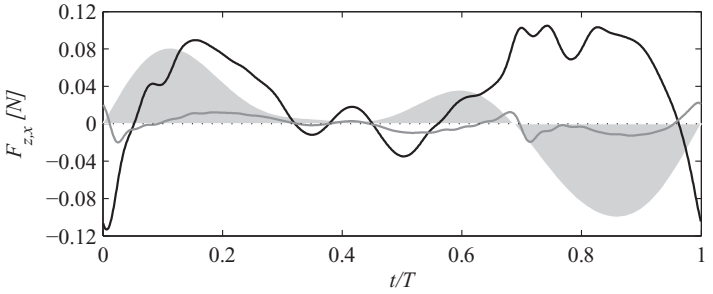

FIG. 3. Hemodynamic forces in the reference axisymmetric case. The base to apex force F_z is shown as a black line and the transversal force F_x is shown as a gray line. The temporal variation of the LV flow rate (not scaled) is reported in the background for reference.

boundary layer at the moving wall and partly dissipates [Fig. 2(a)]. The remaining vortex structure undergoes a winding up and gives rise to an average circulation in the LV as can be seen from the 2D picture on the symmetry plane $y = 0$.

The second diastolic wave, atrial filling, repeats the process and feeds the blood rotation until the end of diastole when the flow is directed toward the outflow tract prepared to be ejected; the pressure is nearly constant with minima corresponding to the cores of the rotating flow [Fig. 2(b)]. During the systolic phase, pressure gradient reverses and drives the rotating blood toward the outflow track, while the remaining 3D vorticity structures are stretched and finally ejected through the aortic orifice, leaving a substantially irrotational flow field inside the LV chamber.

The temporal variation of the longitudinal F_z (base to apex) and of the transversal F_x components of the hemodynamic force for the healthy case computed from the numerical results (11) are reported in Fig. 3. These forces correspond to the pressure gradient integrated on the entire LV volume, not to the viscous stresses that are largely negligible.

The y component of the force is zero because of the model symmetry. For reference, the flow rate is also reported (not in scale); positive and negative values correspond to diastole and systole, respectively. The longitudinal component is about one order of magnitude higher than the transversal one. The time profiles evidence a sharp base-to-apex component between the end of ejection and the beginning of filling, which corresponds to the deceleration of the exiting flow and the acceleration of the entering mitral jet. This phenomenon is known as suction in cardiology and was described as characteristic of systolic-diastolic coupling in healthy cardiac function. A similar but weaker behavior can be observed corresponding with the beginning of the atrial filling wave. Differently, the force from apex to base that develops at the end of filling maintains a nearly steady profile during most of the systolic ejection.

The force is not synchronous with the temporal variation of the ventricular flow rate. This is due to the presence of the convective term, in phase with the flow rate, and of the inertial term, in phase quadrature. The inertial and convective contributions are reported in Fig. 4, together with their approximation given by the integral model described in Sec. IV, and present comparable amplitudes, although they are out of phase. The former dominates during the peak inflow and outflow velocities and the latter during acceleration and deceleration, as expected. The synthetic model provides a good approximation for most of the heartbeat with the exception of the horizontal convective term during late diastole and early systole, which is related to the vortex-induced circulation, as explained before. The model also fails to capture fluctuations characterized by frequencies higher than those related to the LV volumetric changes that are imputable to the intraventricular vorticity dynamics.

B. Reduced amplitude of wall motion

A lack of the wall mobility, with respect to the reference case, can be modeled by reducing the time functions that describe the radial and longitudinal wall motion. This allows investigating the effect

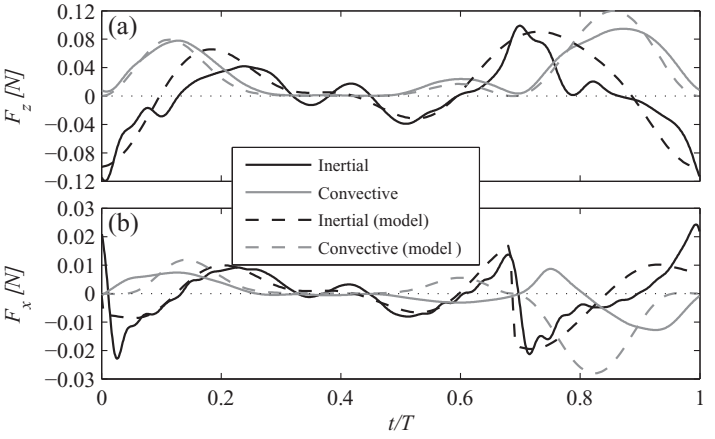

FIG. 4. Contribution to the hemodynamic forces in the reference axisymmetric case. The (a) base to apex force F_z and (b) transversal force F_x are subdivided in the inertial (black line) and convective (gray line) contributions. The corresponding dashed lines are the estimations provided by the global model.

of a reduction of motion amplitude only, mimicking the presence of ideal ischemic diseases without altering the synchrony between the different regions that sometimes accompanies real pathologies.

We first consider the case of reducing the amplitude of the wall motion below the mitral orifice to a partial $R_1(t) = 0.5R_0(t)$ and to a total $R_1(t) = 0$ degree. This ideally corresponds to akinesia in the posterior wall, without changing the dynamics of the other functions (cases 1 and 3 in Table I). The same was performed for the wall below the aortic outflow, $R_2(t) = 0.5R_0(t)$ and $R_2(t) = 0$, corresponding to akinesia in the anterior interventricular septum (cases 2 and 4 in Table I). For both walls, the partial and total amplitude reductions lower the value of ejection fraction from 55% to 51% and 47%, respectively, representing relatively minor pathological conditions. Afterward, we explore the influence of a drastic lower mobility of the entire LV (case 5 in Table I), associated with an EF of 26%, which represents more closely a clinical condition with a critical pathological ischemic state. To this aim, a global lack of contractile function has been introduced by halving the temporal excursion of the radial and longitudinal functions $R_0(t)$ and $H(t)$, maintaining the same end-diastolic (max) values, on top of which a complete ischemia has been introduced locally on the posterior side $R_1(t) = 0$ with $R_2(t) = R_0(t)$.

Figure 5 shows two snapshots of the flow field during the peak of early filling and at the end of diastole for selected indicative cases (1, 3, and 5 in Table I) with a progressive reduction of mobility. Pictures display that the entering jet gets shorter according to the reduced pressure gradient, the increase of the Strouhal number, and the decrease of the vortex formation time (see Table I). As a consequence, the washout of the apical fluid is reduced [10,11]. The smaller penetration of the diastolic flow is the main salient difference that qualitatively alters the overall intraventricular fluid dynamics.

The lowered strength of the entering and exiting jets reflects in a proportional reduction of the hemodynamic forces, shown in Fig. 6 for cases 1, 3, and 5 in Table I. This reduction occurs similarly in both the inertial and convective components of the force (not reported here) that are related to the lower velocity and acceleration of the LV walls. A reduced motion of either the left or right wall of the LV chamber leads to almost identical results in terms of the decrease of the vertical component of the force, with respect to the reference case. Minor differences can be imputable to the local details of the pressure distribution that are related to the asymmetric character of the flow. The time profile of the transversal force is more influenced by whether the symmetry break of wall motion is imposed on the right or the left side. This is associated with a net transversal motion of fluid, which produces an increase of the force toward the less compliant wall during both diastole and systole. This is evidenced by the slight positive bias with respect of the reference profile in Fig. 4.

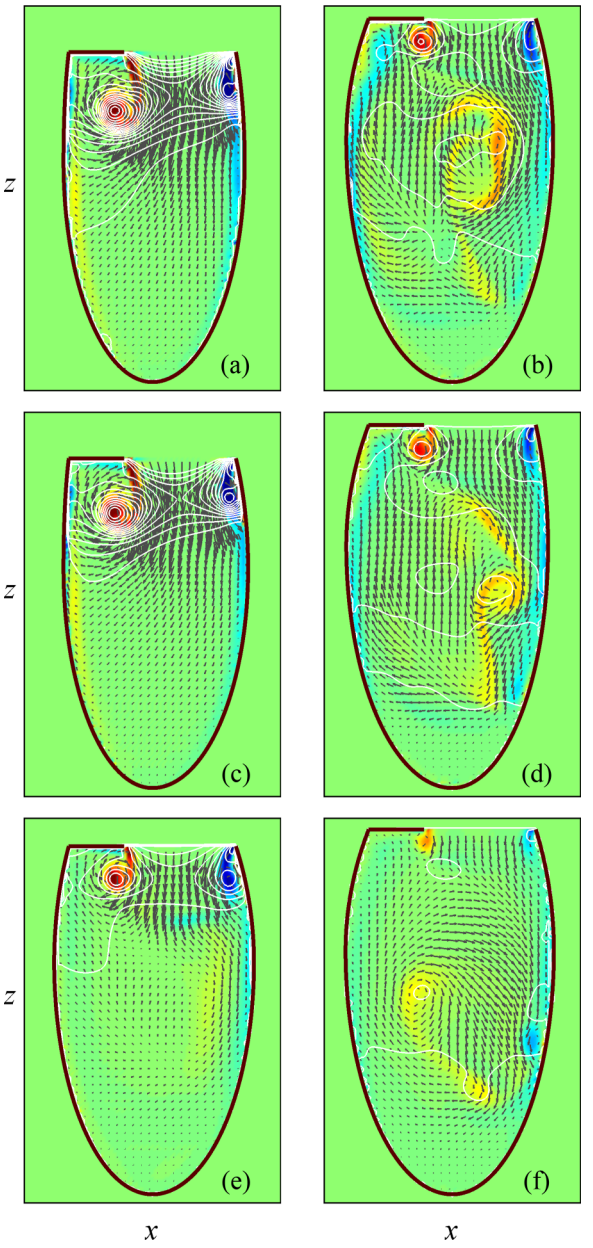

FIG. 5. Flow field in the presence of reduction of the wall motion amplitude. Normal vorticity and in-plane velocity fields are shown on the symmetry plane $y = 0$. Snapshots at diastolic peak ($t = T/8$) and late diastole ($t = 5/8T$) are reported for (a) and (b) case 1, (c) and (d) case 3, and (e) and (f) case 5 (see Table I). Vorticity is color coded for values in the interval $[-200,200]\text{s}^{-1}$, from blue to red. Velocity vectors are down sampled with respect to the computational grid and scaled, to enhance readability. For the pressure field, white isolines are sampled with a pressure difference equal to 10 Pa.

The approximation of the integral model is shown with dashed lines in Fig. 6. The model captures with good accuracy the overall profile of the hemodynamic forces, although some details related to higher-frequency phenomena remain excluded from the global perspective.

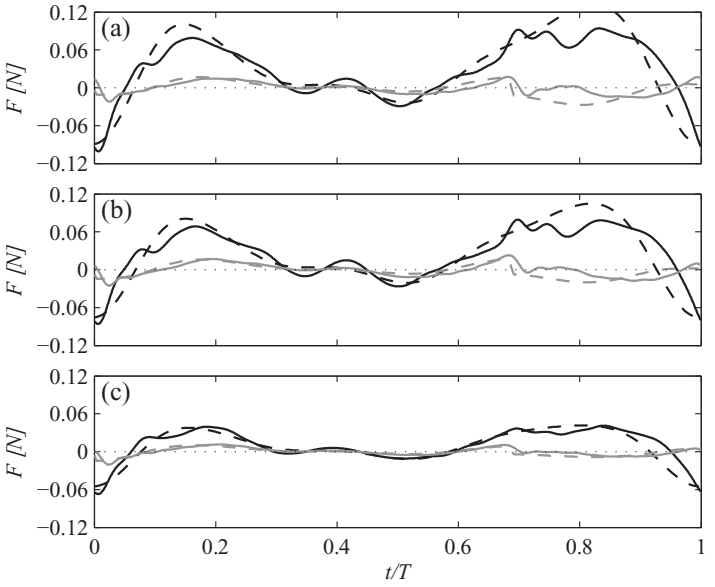

FIG. 6. Hemodynamic forces in the presence of reduction of wall motion amplitude for (a) case 1, (b) case 3, and (c) case 5 (see Table I). The base to apex force F_z is shown as a black line and the transversal force F_x is shown as a gray line. The corresponding dashed lines are the estimations provided by the global model.

C. Altered synchrony of wall motion

Asynchrony was previously documented by clinical studies as a relevant cause affecting the exchange of forces between blood and LV tissue [17,29]. In the ideal context of the present model, asynchrony is introduced by delaying or anticipating the motion of the posterior wall, by simply setting $R_1(t) = R_0(t + T/8)$ or $R_1(t) = R_0(t–T/8)$ without altering the amplitude of the functions (cases 6 and 7 in Table I). In addition to these conditions, we simulated the clinical phenomenon usually called septal flash (case 8 in Table I), which is very common in the presence of conduction pathologies producing LV asynchrony [30]. Septal flash is characterized by a rapid inward-outward motion, varying from 3 to 10 mm, of the septal wall at the very beginning of the systolic contraction and lasting less than 0.1 s [31–33]. It has been modeled here by adding, to the otherwise reference case, a Gaussian inward displacement to the radial dynamics on the septal side $R_2(t) = R_0(t) - a_{SF}\exp[-(\frac{t-t_{SF}}{\tau_{SF}})^2]$, centered at $t_{SF} = 0.75T$, with amplitude $a_{SF} = 3$ mm and duration parameter $\tau_{SF} = 0.03T$. This approximation is not intended to replicate a realistic septal flash but rather to verify the response in terms of hemodynamic forces to a pathologic rapid regional motion.

Figure 7 shows the effect of desynchronization. The vortex at the head of the mitral jet appears longer (shorter) when the filling is anticipated (delayed). However, although the altered timing of events modifies some details and the instantaneous direction of pressure gradient appears slightly deviated, there are no noticeable qualitative differences between the two asynchronous cases and the reference condition in Fig. 2, during the whole heartbeat. The case with septal flash, not reported here, is identical to the reference case for most of the time, with the exception of the period about the flash itself, which, however, does not present vortex formation phenomena. It is a temporary irrotational addition that does not influence the flow field after the phenomenon is terminated.

Figure 8 shows that the time shifts lead to a reduction of the longitudinal force, during the first filling wave and during the systole, according to the reduction of the Strouhal number and vortex formation time (see Table I). The entity of suction between end-systole and early-diastole is drastically reduced in both cases, showing that asynchrony alters the timing of vortex formation, which was shown to affect cardiac intervals [32]. The time profile is also significantly reduced

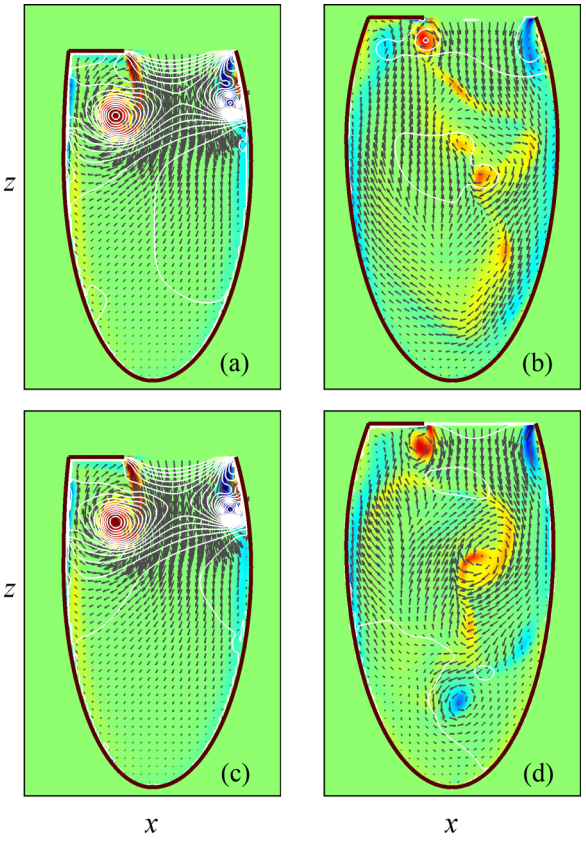

FIG. 7. Flow field in the presence of asynchrony of the wall motion. Normal vorticity and in-plane velocity fields are shown on the symmetry plane $y = 0$. Snapshots at diastolic peak ($t = T/8$) and late diastole ($t = 5/8T$) are reported for (a) and (b) case 6 and (c) and (d) case 7 (see Table I). Vorticity is color coded for values in the interval $[-200,200]\text{s}^{-1}$, from blue to red. Velocity vectors are down sampled with respect to the computational grid and scaled, to enhance readability. For the pressure field, white isolines are sampled with a pressure difference equal to 10 Pa.

after the early filling period, resulting in an almost constant null value in the case of anticipated activation. The relative difference between transversal and longitudinal components is particularly sensitive to desynchronization. During part of the diastole, the two components become comparable in magnitude. During systole, the force is nearly annihilated in the case of delayed contraction, thus blood is pushed upward toward both valves and not preferably toward the aorta as allowed by the small negative F_x. Differently, in the case of anticipated contraction the two force components are nearly comparable, at the transition from diastole to systole. This phenomenon indicates that the activation of contraction pushes blood along an inclined direction, toward the anterior septum, and fails to redirect toward the outflow tract. Both inertial and convective components are modified in a nearly proportional manner, probably as a consequence of the regularity (few harmonics) in the imposed wall motion. These effects are relatively small due to the minimal degree of pathology introduced, as indicated by a reduction of EF from 55% to 50%, as shown in Table I. Although small, the changes are approximately reproduced by the integral model (dashed lines in Fig. 8), especially in terms of relative differences.

The clinical phenomenon of septal flash provokes very large spikes of both components of the hemodynamic force [notice the change of scale in Fig. 8(c)], which are due to the acceleration of

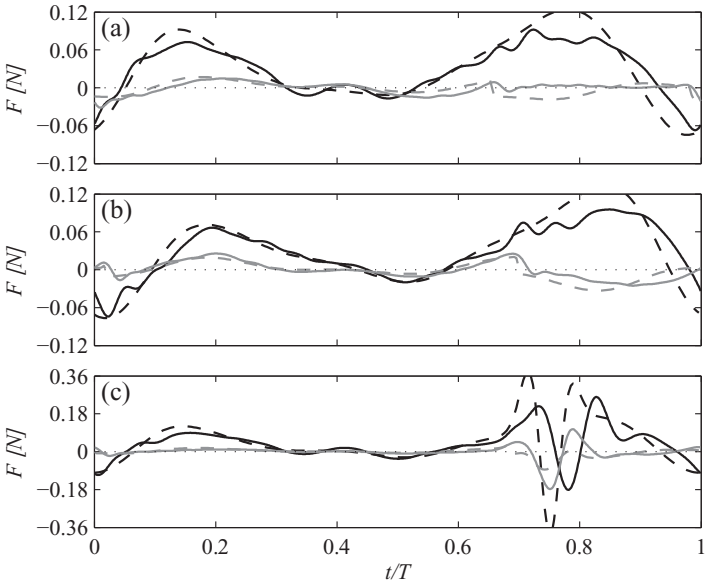

FIG. 8. Hemodynamic forces in the presence of asynchrony of the wall motion for (a) case 6, (b) case 7, and (c) case 8 (see Table I). The base to apex force F_z is shown as a black line and the transversal force F_x is shown as a gray line. The corresponding dashed lines are the estimations provided by the global model. Notice the different vertical scale used in (c).

the column of an incompressible fluid next to the flashing tissue. These spikes are uniquely due to the flow acceleration and are accounted for in the inertial component of the pressure gradient, while the convective component is much smaller. Besides this short period, the force profile remains almost equal to the reference case, telling us that short-lasting flash is essentially an irrotational bulk acceleration and does not create vortex structures able to influence the dynamics afterward. Although short lasting, peak forces are very high. They provoke abnormally high stresses on the LV tissue, which could participate in adaptation feedback.

D. Integral comparison

The approximate model was shown to qualitatively capture the overall profiles of the hemodynamic forces in the different conditions analyzed. A quantification of its accuracy is provided by measuring the relative difference between the force evaluated in the different cases reported in Table I and the value in the reference condition. The relative difference is computed as

$$\Delta = \left[\frac{\int \left(F_x - F_x^{(0)}\right)^2 + \left(F_z - F_z^{(0)}\right)^2 dt}{\int {F_x^{(0)}}^2 + {F_z^{(0)}}^2 dt} \right]^{1/2}, \tag{34}$$

where the superscript (0) stands for the reference condition (case 0, in Table I). Figure 9 shows the relative difference for diastole and systole separately. Some difference between the model and numerical results is noticeable; however, these are relative small, confirming the ability of the model to capture the principal alteration, at least in time-average terms.

High-frequency flow-related fluctuations remain inaccessible to the global model whose harmonic content is limited to that of the wall motion. This can be appreciated from Fig. 10, which compares the time average and the first Fourier harmonic of both the vertical and the horizontal

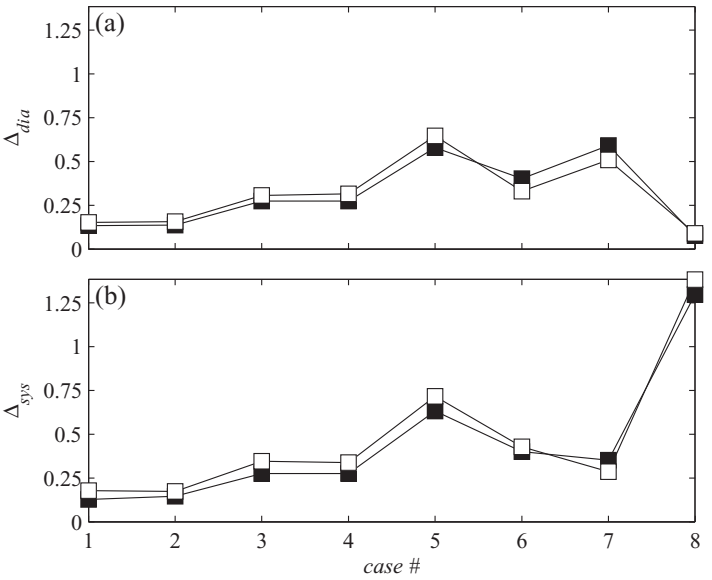

FIG. 9. Relative rms differences of the forces between abnormal cases and the reference one during (a) diastole and (b) systole. Closed markers show numerical results and open markers the synthetic model.

force components. The model partially overestimates the amplitudes; this is more marked for the first harmonic. However, the relative differences between cases are very similar, in agreement with the global result shown in Fig. 9.

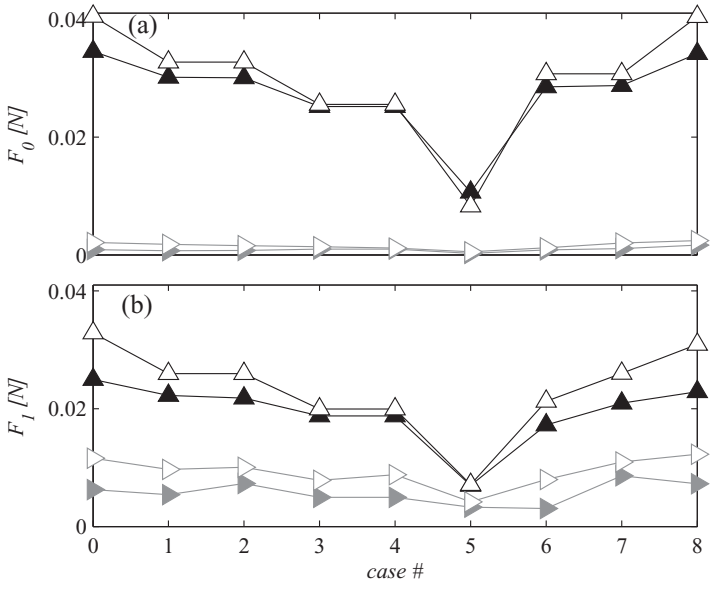

FIG. 10. Fourier analysis of time profiles of hemodynamic forces: (a) zeroth harmonic and (b) first harmonic. Closed markers show numerical results and open markers the synthetic model. The vertical component is represented by upward pointing black markers and the horizontal component by rightward pointing gray markers.

VI. CONCLUSION

Intraventricular pressure gradients were clinically demonstrated to be fundamental in the description of the LV filling-emptying dynamics and the detection of pathologies. The present study investigated via numerical solution of the flow equations in an ideal LV model the relationship between hemodynamics forces (pressure gradients integrated over the LV volume), LV tissue motion, and intraventricular fluid dynamics. It also introduced an original approximate model to estimate hemodynamic forces from information commonly recorded in cardiac imaging examinations when the detailed knowledge of intraventricular fluid dynamics is not available.

The normal time course of the forces reflects the asymmetry between the filling and ejection processes. Diastole is anticipated by a deep base-to-apex force component (suction) that terminates right after the beginning of filling; contrarily, systole is characterized by an apex-to-base thrust, which is nearly constant from the end of diastole to the final part of systole, when it throws blood into the new suction. These findings match clinical observations and confirm that the transversal component of the force is one order to magnitude smaller than the longitudinal one.

Pathologic changes were investigated, within the limitation of the LV model, to give some initial understanding of how alterations of tissue motion are reflected in terms of hemodynamic forces. Results clearly show that a reduction of the LV wall mobility, as could be associated with ischemic diseases, leads to an almost proportional reduction of hemodynamics forces, in both the longitudinal and transversal directions. In contrast, regional asynchrony modifies the time course of the hemodynamic forces and the ratio between the longitudinal and transversal components. Asynchronous regional wall motion modifies the direction along which the blood is thrust. In particular, rapid local phenomena, such as septal flash, produce exceptionally high forces provoking nonphysiological stresses on LV tissues.

The approximate model, based on integral momentum and mass balance, demonstrated a good reliability to reproduce the main properties of the global hemodynamic force vector and especially the relative differences in the different conditions. The model is unable to capture the force fluctuations with a frequency higher than those given by the imposed wall motion, such as those due to the intraventricular vortex dynamics that cannot be accounted for in the integral balance.

Hemodynamic forces computed using the synthetic model may provide initial physics-based indications regarding the global flow-tissue interaction in the LV based on quantities, such as tissue motion and inflow-outflow velocity, that are commonly measured in clinical cardiology by medical imaging technology. Therefore, this simple model represents a step for integrating fluid dynamics in the clinical examination and improving the diagnosis of the LV function.

ACKNOWLEDGMENT

The study was partially supported by Italian government Project (Progetti di Rilevante Interesse Nazionale) No. Prot.N.2012HMR7CF.

[1] D. Levy, S. Kenchaiah, M. G. Larson, E. J. Benjamin, M. J. Kupka, K. K. L. Ho, J. M. Murabito, and R. S. Vasan, Long-term trends in the incidence of and survival with hearth failure, New-Engl. J. Med. **347**, 1397 (2002).

[2] K. Chatterjee and B. Massie, Systolic and diastolic heart failure: differences and similarities, J. Cardiac Fail. **13**, 569 (2007).

[3] M. Genet, L. C. Lee, B. Baillargeon, J. M. Guccione, and E. Kuhl, Modeling pathologies of diastolic and systolic heart failure, Ann. Biomed. Eng. **44**, 112 (2016).

[4] L. H. Opie, P. J. Commerford, B. J. Gersh, and M. A. Pfeffer, Controversies in ventricular remodelling, Lancet **367**, 356 (2006).

[5] P. P. Sengupta and J. Narula, Reclassifying heart failure: predominantly subendocardial, subepicardial, and transmural, Heart Fail. Clin. **4**, 379 (2008).
[6] A. Pasipoularides, Mechanotransduction mechanisms for intraventricular diastolic vortex forces and myocardial deformations: Part 1, J. Cardiovasc Trans. Res. **8**, 76 (2015).
[7] G. Pedrizzetti, G. La Canna, O. Alfieri, and G. Tonti, The vortex- an early predictor of cardiovascular outcome?, Nat. Rev. Cardiol. **11**, 545 (2014).
[8] R. Mittal, J. H. Seo, V. Vedula, Y. J. Choi, H. Liu, H. H. Huang, S. Jain, L. Younes, T. Abraham, and R. T. George, Computational modeling of cardiac hemodynamics: current status and future outlook, J. Comput. Phys. **305**, 1065 (2016).
[9] G. Pedrizzetti and F. Domenichini, Left ventricular fluid mechanics: the long way from theoretical models to clinical applications, Ann. Biomed. Eng. **43**, 26 (2015).
[10] C. J. Carlhäll and A. F. Bolger, Passing strange: flow in the failing ventricle, Circ. Heart Fail. **3**, 326 (2010).
[11] M. Gharib, E. Rambod, A. Kheradvar, D. J. Sahn, and J. O. Dabiri, Optimal vortex formation as an index of cardiac health, Proc. Natl. Acad. Sci. USA **103**, 6305 (2006).
[12] J. O. Mangual, A. De Luca, E. Kraigher-Krainer, L. Toncelli, A. Shah, S. Solomon, G. Galanti, F. Domenichini, and G. Pedrizzetti, Comparative numerical study on left ventricular fluid dynamics after dilated cardiomyopathy, J. Biomech. **46**, 1611 (2013).
[13] J. W. Son, W. J. Park, J. H. Choi, H. Houle, M. A. Vannan, G. R. Hong, and N. Chung, Abnormal left ventricular vortex flow patterns in association with left ventricular apical thrombus formation in patients with anterior myocardial infarction: a quantitative analysis by contrast echocardiography, Circ. J. **76**, 2640 (2012).
[14] H. Abe, G. Caracciolo, A. Kheradvar, G. Pedrizzetti, B. K. Khandheria, and J. Narula, Left ventricular efficiency in heart failure is related to the intracavitary vortex strength during isovolumic contraction, Eur. Heart J. Cardiovasc. Imag. **14**, 1049 (2013).
[15] V. Cicchitti, F. Radico, F. Bianco, S. Gallina, G. Tonti, and R. De Caterina, Heart failure due to right ventricular apical pacing: the importance of flow patterns, Europace **18**, 1679 (2016).
[16] A. Pasipoularides, Mechanotransduction mechanisms for intraventricular diastolic vortex forces and myocardial deformations: part 2, J. Cardiovasc. Trans. Res. **8**, 293 (2015).
[17] S. Cimino, G. Pedrizzetti, G. Tonti, E. Canali, V. Petronilli, L. De Luca, C. Iacoboni, and L. Agati, In vivo analysis of intraventricular fluid dynamics in healthy hearts, Eur. J. Mech. B **35**, 40 (2012).
[18] J. Eriksson, A. F. Bolger, T. Ebbers, and C. J. Carlhäll, Assessment of left ventricular hemodynamic forces in healthy subjects and patients with dilated cardiomyopathy using 4D flow MRI, Physiol. Rep. **4**, e12685 (2016).
[19] G. Pedrizzetti, A. R. Martiniello, V. Bianchi, A. D'Onofrio, P. Caso, and G. Tonti, Cardiac fluid dynamics anticipates heart adaptation, J. Biomech. **48**, 388 (2015).
[20] B. Baccani, F. Domenichini, and G. Pedrizzetti, Vortex dynamics in a model left ventricle during filling, Eur. J. Mech. B **21**, 527 (2002).
[21] F. Domenichini and G. Pedrizzetti, Asymptotic model of fluid–tissue interaction for mitral valve dynamics, Cardiovasc. Eng. Technol. **6**, 95 (2015).
[22] J. H. Seo, V. Vedula, T. Abraham, A. C. Lardo, F. Dawoud, H. Luo, and R. Mittal, Effect of Mitral Valve on the Diastolic Flow Pattern, Phys. Fluids **26**, 121901 (2014).
[23] F. Domenichini and G. Pedrizzetti, Intraventricular vortex flow changes in the infarcted left ventricle: numerical results in an idealised 3D shape, Comput. Methods Biomech. Biomed. Eng. **14**, 95 (2011).
[24] G. Pedrizzetti, F. Domenichini, and G. Tonti, On the left ventricular vortex reversal after mitral valve replacement, Ann. Biomed. Eng. **38**, 769 (2010).
[25] F. Domenichini, On the consistency of the direct forcing method in the fractional step solution of the Navier–Stokes equations, J. Comput. Phys. **227**, 6372 (2008).
[26] J. Eriksson, A. F. Bolger, T. Ebbers, and C. J. Carlhäll, Left ventricular hemodynamic forces are altered in patients with dilated cardiomyopathy, J. Cardiovasc. Magn. Res. **17**, P282 (2015).
[27] P. J. Kilner, G. Z. Yang, A. J. Wilkes, R. H. Mohiaddin, D. N. Firmin, and M. H. Yacoub, Asymmetric redirection of flow through the heart, Nature (London) **404**, 759 (2000).

[28] G. Pedrizzetti and F. Domenichini, Nature optimizes the swirling flow in the human left ventricle, Phys. Rev. Lett. **95**, 108101 (2005).

[29] G. Pedrizzetti, A. R. Martiniello, V. Bianchi, A. D'Onofrio, P. Caso, and G. Tonti, Changes in electrical activation modify the orientation of left ventricular flow momentum: novel observations using echocardiographic particle image velocimetry, Eur. Heart J. Cardiovasc. Imag. **17**, 203 (2016).

[30] B. Corteville, J. De Pooter, T. De Backer, M. El Haddad, R. Stroobandt, and F. Timmermans, The electrocardiographic characteristics of septal flash in patients with left bundle branch block, Europace (to be published).

[31] M. Čikeš, B. Bijnens, Z. Đurić, M. L. Benčič, I. Gošev, V. Velagić, H. Gašparović, D. Miličić, and B. Biočina, Detecting volume responders prior to implantation of a cardiac resynchronization therapy device via minithoracotomy: the septal flash as a predictor of immediate left ventricular reverse remodeling, Heart Surg. Forum **12**, E362 (2009).

[32] S. I. Sarvari, M. Sitges, M. San, J. M. Tolosana Viu, T. Edvardsen, T. M. Stokke, L. Mont, and B. Bijnens, Left ventricular dysfunction is related to the presence and extent of a septal flash in patients with right ventricular pacing, Europace (to be published).

[33] G. Goliasch, K. Goscinska-Bis, G. Caracciolo, A. Nakabo, G. Smolka, G. Pedrizzetti, J. Narula, and P. P. Sengupta, CRT imporves LV filling dynamics. Insights from echocardiography particle imaging velocimetry, J. Am. Coll. Cardiol. Imaging **6**, 704 (2013).